Titania Hybrid Carbon Spherogels

for Photocatalytic Hydrogen Evolution

Jorge Torres-Rodríguez[#,a,b], Stephen Nagaraju Myakala[#,c], Miralem Salihovic[a], Maurizio Musso[a], Nicola Hüsing[a,b], Dominik Eder[c], Volker Presser[d,e,f], Alexey Cherevan[c,*] and Michael S. Elsaesser[a,*]

[a] *Paris-Lodron-University of Salzburg, Department of Chemistry and Physics of Materials, 5020 Salzburg, Austria*

[b] *Salzburg Center for Smart Materials, 5020 Salzburg, Austria*

[c] *TU Wien, Institute of Materials Chemistry, 1060 Wien, Austria*

[d] *INM – Leibniz Institute for New Materials, 66123 Saarbrücken, Germany*

[e] *Department of Materials Science and Engineering, Saarland University, 66123 Saarbrücken, Germany*

[f] *Saarene, Saarland Center for Energy Materials and Sustainability, 66123 Saarbrücken, Germany*

* Corresponding authors' emails:

michael.elsaesser@sbg.ac.at (ME); alexey.cherevan@tuwien.ac.at (AC)

[#] These authors contributed equally

Keywords:

hybrid aerogels; nanoporous materials; hollow carbon spheres; photocatalysis; hydrogen evolution reaction; titania

Abstract:

Recently, carbon spherogels have been introduced as a novel monolithic aerogel composed of hollow spheres. This material is conveniently obtained via polystyrene (PS) sphere templating. In the present study, we apply a water-soluble titania precursor (titanium(IV) bis(ammonium lactate) to the aqueous sol-gel synthesis based on resorcinol-formaldehyde (RF) to effectively encapsulate titania. In this way, a very high mass loading of up to 59 mass% of titania can be confined strictly to the inside of the hollow carbon spheres. In the final synthesis step, carbonization at 800 °C has three simultaneous effects: Transformation of the RF coating on PS into microporous carbon, PS template removal by decomposition, and formation of titania due to precursor dissociation. A deliberate tuning of the microporous carbon shell, accessibility of the titania, titania amount, and titania's polymorph is further demonstrated by thermal treatment under a carbon dioxide atmosphere. In contrast to non-tuned or TiC-containing carbon spherogels, CO_2 activation of the composites results in a three orders of magnitude rise of their photocatalytic activity towards hydrogen evolution reaction, which we evaluate using flow and batch reactors. We further show that this effect is related to the partial etching of the carbonaceous shell, which renders the TiO_2 surface accessible to the reactants in the solution and allows for an efficient hole scavenging. Given the simplicity of the hybrid carbon spherogel (HCS) composite fabrication, the high degree of control of their morphological characteristics, and the striking effects of CO_2-activation on performance, we strongly believe that our results will interest a broad scientific community and contribute to the development of similar carbon-inorganic composites.

Introduction

Phasing out our present-day use of carbonaceous energy sources, such as coal, oil, and gas, is a key to enabling a more sustainable and more peaceful future for humankind.[1, 2] Using non-renewable energy sources has caused a dramatic increase in the carbon dioxide concentration in the earth's atmosphere, leading to global warming and air pollution (by fine dust and aerosol soot).[3] Green hydrogen, produced by water splitting[4] powered by renewable energy (photovoltaics, wind energy, or geothermal energy), could serve as a promising alternative energy carrier for direct use (fuel cells) or interstage for synthetic fuel production.[5, 6] Furthermore, direct hydrogen evolution by photocatalytic water splitting represents an essential and optional pathway.

The design of novel catalyst systems is under immense investigation, not only focusing on new materials combinations but also concerning efficiency, long-term stability, and eco-friendliness.[7, 8] The design of core-shell materials, fashioned by a porous carbon scaffold and an active titanium-containing compound (e.g., titania) is one of the most promising strategies in photocatalysis today.[9] Hybrid carbon nanomaterials are accessible by bottom-up strategies (e.g., sol-gel, casting) or top-down approaches such as atomic layer deposition.[10-12] Another way of obtaining carbon hybrid materials is by in situ conversion of, for example, metal carbides and MXenes.[13, 14] Encapsulating metal oxides into a porous, hollow carbon sphere scaffold also enables their catalytic activity, electrical dissipation, good accessibility, and leaching protection. Various templating approaches, usually based on spherical silica[15] or polymers combined with sol-gel or hydrothermal synthesis,[16] were developed to obtain hollow carbon sphere powders.[17] Monolithic and reversibly compressible carbon spherogels were developed using a polystyrene sphere templated gelation of resorcinol and formaldehyde.[18] Further functionalization with metal oxides can be achieved by thermally triggered impregnation with molten

compounds, for example, sulfur,[19] germanium,[20] or copper[21]. Specific crystallization in the sphere interiors (ship-in-the-bottle principle), can be achieved by selective etching, spray pyrolysis, or layer-by-layer assembly. Via confined interfacial copolymerization, Au-seeds can be incorporated into hollow carbon spheres.[22] The most elegant routes feature a one-pot synthesis to built-up hybrid hollow sphere materials.[23-25]

This study introduces an advanced, one-pot template-assisted approach to preparing titania encapsulated carbon spherogels. This new methodology allows us to build *in-situ* hybrid nanostructured core-shell materials with a deliberately controlled morphology, a tunable titania loading, and extraordinary structural and chemical homogeneity. As the sol composition, choice of solvents, pH value, and catalyst amount severely affect the gelation of resorcinol-formaldehyde, identifying a water-soluble titania precursor was a fundamental prerequisite for a successful protocol. Our strategy benefits from low-temperature sol-gel chemistry, low equipment costs, and concomitant (more environmentally friendly than silica templating) template removal during carbonization. Our work also investigates the effect of two different post-processing approaches (CO_2 etching and thermal annealing under Ar atmosphere), on the physicochemical properties of the hybrid TiO_2/carbon spherogels and their impact on the light-driven hydrogen evolution efficiency. Finally, we show that the accessibility of TiO_2 nanocrystals plays an essential role in allowing for quick utilization of the photogenerated holes and that the carbonaceous shell encapsulating the titania layer can act as an electron mediator, allowing for their extraction and transport to the reduction sites.

Experimental

Chemicals

Technical grade acetone (> 99%) was purchased from VWR. Styrene (≥ 99%), titanium(IV) bis(ammonium lactate) dihydroxide solution (50 mass% in H_2O), polyvinylpyrrolidone (average molar weight 40,000), resorcinol (99%), formaldehyde solution (37% stabilized with 10% methanol) and sodium carbonate were acquired from Sigma Aldrich and used without further purification. Potassium persulfate was supplied by Honeywell Fluka.

Synthesis of Hybrid Carbon Spherogels

The polystyrene (PS) spheres were synthesized according to Du *et al.*[26] by an emulsion polymerization reaction of styrene with potassium persulfate as an initiator and polyvinylpyrrolidone as a stabilization agent. The obtained PS sphere solution (average diameter: 275±3.5 nm, *Supporting Information*, **Figure S1**) was diluted to a final concentration of 9% by mass. This aqueous PS solution was used as a templating agent for the carbon spherogels. To prepare the organic gels, the resorcinol (R, carbon source) was dissolved in 25 g of 9% PS solution under mild magnetic stirring for 10 min. Consecutively, the titanium precursor titanium(IV) bis(ammonium lactate) dihydroxide (1.2 g (LOW), 2.5 g (MED), and 3.7 g (HIGH)) was dripped into the solution and kept stirring for an additional 10 min. In the next step, formaldehyde (F) was added at a molar ratio of F/R = 1.5 followed by the addition of the $NaCO_3$ (C) to catalyze the reactions. The final F/R/C/Ti was 1.5/52/0.6. Then, the pH was adjusted to 3 using a 2N HNO_3 aqueous solution, and the mixture was stirred for 1 h. Afterward, the mixture was poured and sealed in cylindrical glass vials and placed in an oven for aging for 7 d at 80 °C. In the next step, the gels were immersed in acetone (fresh acetone was exchanged every 24 h, 3 times) to remove the unreacted species and by-products. Upon the solvent exchange pro-

cedure, the wet gels were dried by supercritical extraction with CO_2 at 60 °C and 11 MPa. Finally, the obtained organic aerogels were carbonized in a tube furnace (alumina tube) in a controlled Ar atmosphere (75 NL h^{-1}) at 800 °C with a heating ramp of 60 °C h^{-1}, and a dwell time of 2 h. Upon cooling at room temperature, monolithic carbon spherogels were obtained. Post-synthetic heat treatment was followed by one of the following methods: (1) Physical activation with carbon dioxide (quality 4.5) in a tube furnace (800 °C, 600 °C h^{-1}, 30 min, 1 NL min^{-1} CO_2 flow) or (2) annealing under argon atmosphere at 1100 °C for 120 min (Ar quality 5.0).

Materials characterization

The surface morphology of the carbon spherogels was analyzed by scanning electron microscopy (SEM), recorded with a Zeiss Ultra Plus instrument, using an in-lens secondary electron detector and an acceleration voltage of 15 keV. Transmission electron microscopy (TEM) images were taken with a JEOL JEM F200 microscope, equipped with a cold field emission source and a TVIPS F216 2000x2000 CMOS camera. The TEM images were obtained using an electron acceleration voltage of 200 keV.

Nitrogen sorption isotherms were recorded on a Micromeritics ASAP 2420 surface area and porosity analyzer at -196 °C and in a relative pressure range p/p_0 from 10^{-7} to 1. Before analysis, the samples were degassed at 300 °C for 12 h under vacuum (2.67 kPa). The obtained isotherms were analyzed using the MicroActive (Version 5.0) software. The usage of the non-local density functional theory (HS-2D-NLDFT), allows the determination of the samples' specific surface area (SSA) as well as pore size distribution (PSD).[27, 28]

Raman spectra were collected in the spectral range between 100 cm^{-1} to 3500 cm^{-1} with a 532 nm laser excitation wavelength and a laser power of 4 mW on the sample. A Thermo Scientific DXR2 Raman microscope was used, equipped with a confocal microscope BX41 (Olympus Corp.) and a 10× objective with 0.25 numeric aperture, delivering a laser spot diameter of approximately 2.1 µm and a, therefore, laser intensity on the sample of about 1.2 mW μm^{-2}. The full range grating with 900 lines mm^{-1} allowed with a 50 µm pinhole-like entrance slit to the spectrometer a spectral resolution (equivalent to the FWHM of the instrumental line width) of about 1 cm^{-1}.

The thermogravimetric analysis (TGA) was carried out on a Netzsch STA 449 F3 Jupiter instrument. The samples were heated at a rate of 10 °C min^{-1} from 20 °C to 1000 °C under Ar atmosphere.

The particle size distribution of the PS spheres was analyzed by dynamic light scattering (DLS), using a Malvern Zetasizer instrument. Each measurement consisted of three separate DLS measurements with 30 sub-runs each.

The crystallite size (D) was determined from the X-ray line broadening using Scherrer´s equation:

$$D = \frac{K\lambda}{\beta cos\theta}$$

where *K* is the shape factor (0.94), λ is the X-ray wavelength (0.154 nm), β is the line broadening at half of the maximum intensity in radians (full width at half maximum: FWHM). The FWHM values were determined by fitting the XRD pattern peaks for the lattice planes of the corresponding anatase and rutile phases after subtraction of the line broadening of the instrument.

Photocatalytic experiments

The hydrogen evolution experiments were carried out using a side-illumination slurry type reactor (total volume of 9 mL) equipped with a monochromatic UV LED light source with an incident light intensity of 0.49 W centered at 365±6 nm (196 mW cm^{-2}, SOLIS, Thorlabs). The experiments were performed either in a batch-type or a flow-type mode. The temperature of the reactor solution was maintained at 15 °C using a water-cooling system (Lauda). The reaction solution was stirred at 650 rpm throughout the experiment. In a single run, 1 mg of the powdered photocatalyst was first dispersed in 2 mL of 1:1 by volume MeOH:H_2O mixture by ultrasonication for 180 s. The mixture was transferred to the reactor; 125 µL of aqueous H_2PtCl_6 solution was added, corresponding to 10 µg (1 mass%) Pt employed here as H_2 evolution co-catalyst. The solution was purged with Ar (flow rate of 15 mL min^{-1}, controlled with a mass flow controller from MCC-Instruments) to remove dissolved oxygen before starting the illumination. In a batch-type mode, products of the photocatalytic reaction accumulated in the reactor volume; the amount of evolved H_2 was analyzed with a GC-2030 (Shimadzu) instrument using a Micropacked-ST Column (ShinCarbon) and a barrier discharge ionization detector (BID). Sampling was done using a gas-tight syringe (Hamilton). In a flow-type mode, to deliver the products of the photocatalytic reaction to the detector, the reactor was continuously purged with Ar carrier gas at a flow rate of 15 mL min^{-1}. The gaseous H_2 was detected directly in the stream by an online gas analyzer (X-stream, Emerson Process Management) equipped with a thermal conductivity detector. For both detectors, H_2 concentrations were deduced based on a multilevel calibration. A typical H_2 evolution profile (*e.g.,* in **Fig. 6B**, Y-axes to be the rate of H_2 evolution) obtained in flow-mode includes an induction period (increasing H_2 evolution rate during the first 10 min) that is due to the fact the H_2 gas first needs to fill the dead volume (e.g., reactor volume, tubing volume) to reach the detector. After this induction,

H_2 evolution reached a stable rate, which speaks for stable HER performance. In contrast, when the rate changes over time, (de)activation of the photocatalytic system can be deduced.[29, 30] When the illumination stopped, the signal returned to the baseline.

Results and discussion

Preparation of hybrid titania carbon spherogels

We recently reported a robust synthetic pathway to produce monolithic carbon spherogels in aqueous media.[25] This methodology is based on the gelation of resorcinol-formaldehyde assisted with polystyrene spheres as a template.[18, 31] The preparation of metal-oxide-loaded carbon spherogels based on this route requires the addition of an organometallic or metal salt precursor to the sol-gel process. For instance, the common use of metal-acetylacetonate precursors is linked to low water solubility and low metal loadings. These aspects hinder the feasibility of developing a flexible method based on these compounds. For example, $Ti(IV)(acac)_2(OiPr)_2$ presents high solubility in isopropanol (up to 50 mass%). However, the alcohol-water mixture in the sol-gel process provokes negative effects such as partial precipitation, sample inhomogeneity, or even no gelation. We overcame these issues by using the water-soluble titanium(IV) bis(ammonium lactate) dihydroxide.

The present study introduces preparing a set of hybrid carbon spherogel samples with varying encapsulated TiO_2 amounts. In a typical synthesis, 1.2-3.7 g of $C_6H_{10}O_8Ti$ $(NH_4)_2$ is added to a sol consisting of resorcinol (R), formaldehyde (F), and 9 mass% polystyrene sphere aqueous solution. A general scheme of the synthetic protocol is shown in **Fig. 1**. In detail, the surface of monodisperse, 275-nm-sized, negatively charged (*Supporting Information*, **Fig. S1**; prepared by emulsion polymerization) polystyrene spheres serve as preferential sites for the attachment of resorcinol-titanium (IV) precursor species. Subsequently, the addition of formal-

dehyde generates a polymeric RF layer around the spheres that eventually condenses, followed by the formation of a wet gel of interconnected spherical particles (**Fig. 1**). At this stage, the correct PS-to-RF ratio is critical, and an appropriate adjustment of the final pH since the morphology of the particles varies drastically with the interplay of these synthetic parameters. For instance, at PS concentrations below 9 mass%, we see a bimodal morphology of spheres and RF nanoparticles (*Supporting Information*, **Fig. S2A-C**). At pH values above 3, dense aggregates with an inner layer of TiO_2 and dispersed TiO_2 nanocrystals are obtained (*Supporting Information*, **Fig. S2A-B**). The optimum synthetic conditions for homogeneity, core-shell particles arranged in a 3D network, and wet gel stability were met for an aqueous solution with 9 mass% PS and a pH value of 3. The resulting wet gels are subsequently dried with supercritical carbon dioxide to avoid severe shrinkage effects and carbonized under Ar atmosphere. Here, within a one-step process, three transformations occur: 1) RF transformation to carbon concomitantly with micropore formation, 2) titania-precursor decomposition yielding titania crystallites, 3) and PS template removal due to thermal decomposition.

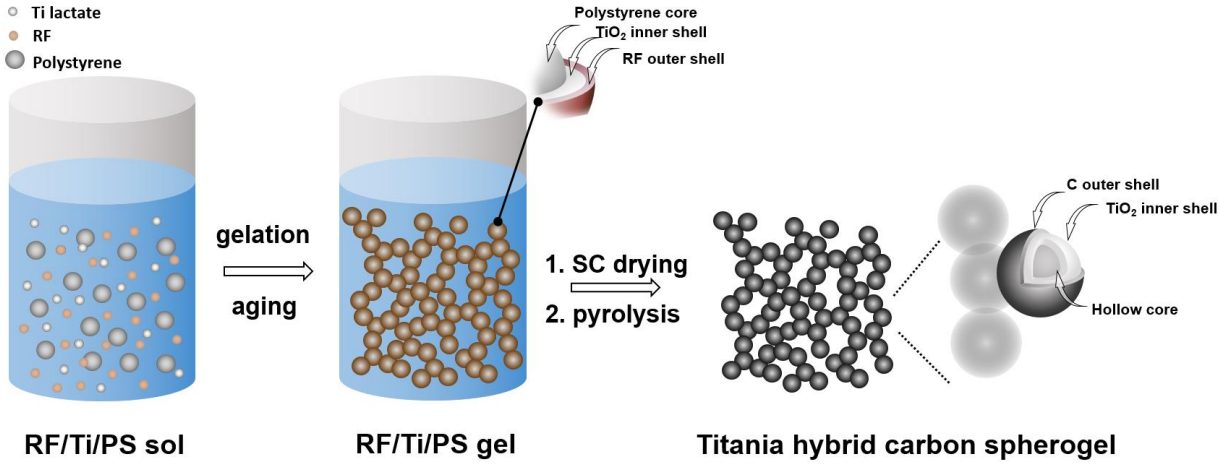

Fig. 1: Schematic representation of the aqueous synthetic pathway to hybrid carbon spherogels composed of hollow titania/carbon spheres starting from polystyrene colloids as templating agents, resorcinol and formaldehyde as organic precursors, and dihydroxy bis(ammonium-lactato)titanium(IV) as titania source (SC = supercritical drying with carbon dioxide).

A set of samples using the optimized synthesis parameters (pH 3 and 9 mass% template concentration) with three different TiO_2 loadings (LOW / MED / HIGH) were prepared. All samples present an extraordinary homogeneity, as shown by scanning electron micrographs (**Fig. 2**). A homogeneous 3D assembly is obtained at the optimized conditions with very well-defined hollow spheres invariant with the TiO_2 loading. The ability of the carbon spherogel to maintain the morphology, size, and shape irrespective of the titania loading is a strong advantage when matching the composition to a specific application.

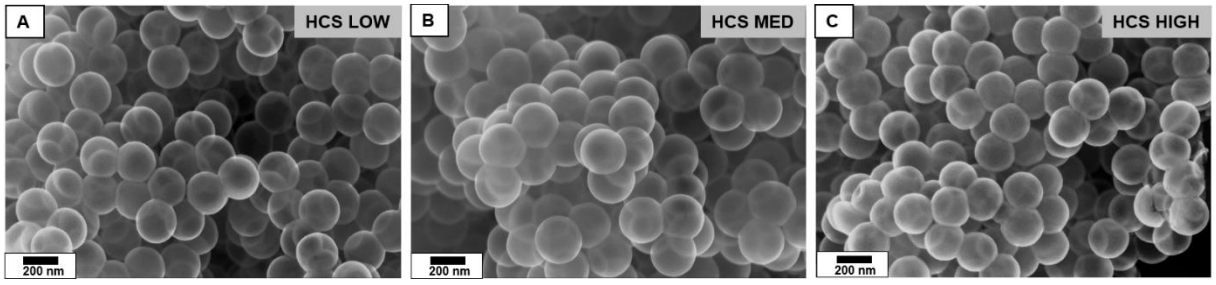

Fig. 2: Scanning electron micrographs of low, medium, and high titania-loaded spherogels as obtained (A-C).

For all these materials, the transmission electron micrographs reveal a hybrid carbon spherogel (HCS) structure composed of hollow spheres with an inner titania layer surrounded by carbon (**Fig.3A-C**). Using polystyrene spheres with 275 nm diameter, we obtained hybrid carbon spherogel samples with an interior diameter between 220 nm and 237 nm, which indicates a typical slight shrinkage due to carbonization.

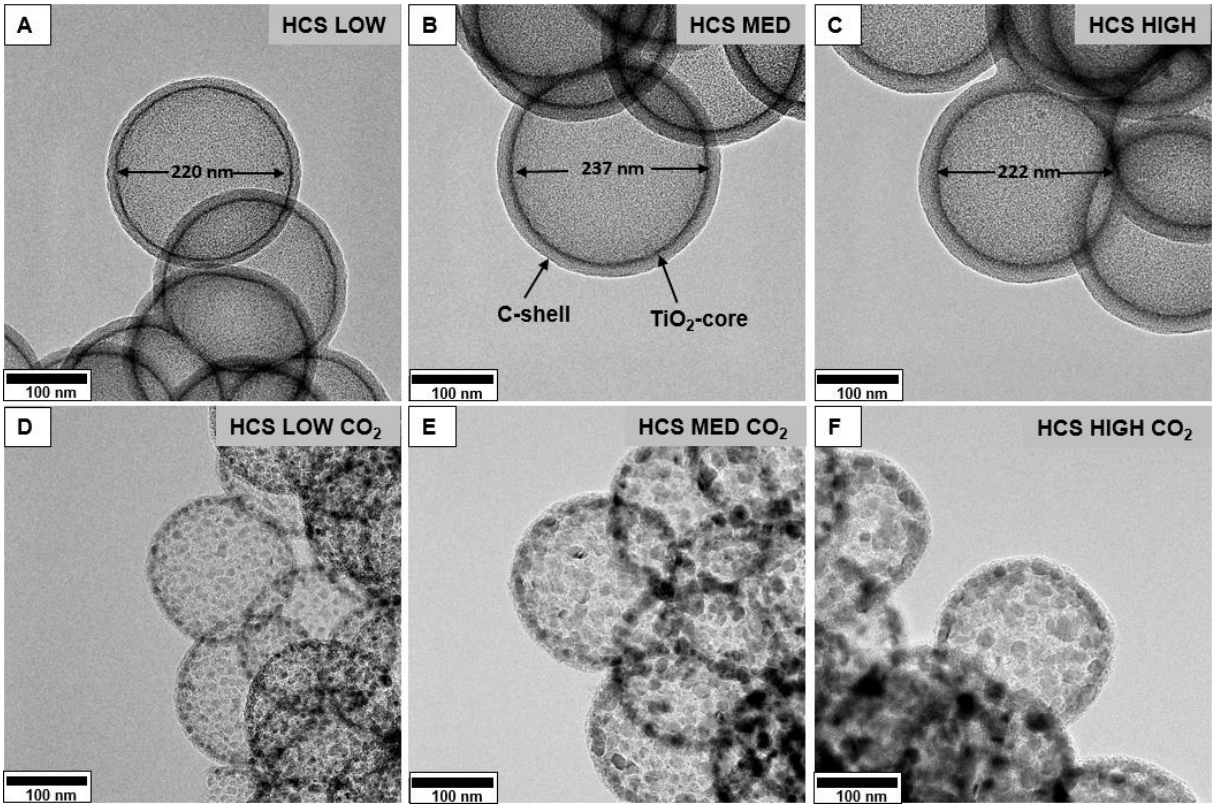

Fig. 3: Transmission electron micrographs of low, medium, and high titania-loaded carbon spherogels (A-C: as obtained; D-F: 30 min activated with carbon dioxide at 800 °C).

The thermogravimetric analysis (*Supporting Information*, **Fig. S3**) under synthetic air up to 1000°C revealed a residual of 31 mass%, 44 mass%, and 59 mass% (LOW, MED, HIGH), respectively. These very high titania loading values have been enabled by using the water-soluble Ti-lactate precursor system. For comparison, our previous work using Ti-acac was limited to a loading of just 22 mass% of titania.[25]

Elemental analysis by STEM-EDX for the elements Ti, C, and O (*Supporting Information*, **Fig. S4**) verifies the presence of a continuous, nano-crystalline, uniformly-sized titania layer surrounded by carbon for low, medium, and high loaded samples. The different titania contents are also supported by the profile scan plots (*Supporting Information*, **Fig. S4**) where a proportional decrease in the C profile is evident as the Ti content increases. The HCS LOW sample shows a dominant C concentration with significantly small Ti, and O content. In contrast, in

HCS MED, the intensity is similar for all the components, and in the high titania-loaded sample (HCS HIGH), the Ti signal appears stronger than C and O.

Post-synthesis thermal treatment and physical activation

For photocatalysis (and many other applications), the accessibility of titania through the microporous carbon shell is a critical factor. Commonly, thermal treatment can be applied to improve the permeability of the porous carbon shell. For example, this can be done by generating micropores via long-term carbonization[32] or physical activation with carbon dioxide.[33, 34] Besides increasing the micropore content by carbon etching, the relative amount of titania (the titania-to-carbon ratio) can also be increased by activation as, unlike titania, only carbon species are removed.

To generate a higher amount of micropores within the carbon layer, the obtained TiO_2-carbon spherogels are treated via two different approaches: a) annealing at 1100 °C under Ar atmosphere for 120 min or b) CO_2 treatment at 800 °C for 30 min (labeled with 'AR' or 'CO_2', respectively). As shown in *Supporting Information*, **Fig. S5A**, the samples treated under Ar resulted in a slight crystallite size growth compared to the as-obtained counterpart (HCS LOW AR). The X-ray diffraction analysis of the Ar treated samples revealed that such crystals belong to the TiC phase (*Supporting Information*, **Fig. S5B**).

After CO_2 activation (hereafter HCS LOW CO_2, HCS MED CO_2, and HCS HIGH CO_2), the samples showed an increase in the TiO_2 particle size, as visualized in TEM EDX images (**Fig. 4**), that varies with the initial TiO_2 amount in the range of 8 nm to 27 nm. This tendency can be correlated to the availability of TiO_2. The low available TiO_2 amount on the HCS LOW CO_2 limits the aggregation and hinders particle growth. Conversely, the particle growth will be favored in the samples with higher initial TiO_2 content because of a larger amount of available TiO_2, as in the

HCS MED CO_2 (18 nm) and HCS HIGH (27 nm). Not only was the particle size affected by the initial TiO_2 content but also the crystalline phase composition. At low TiO_2 content, the sample is composed solely of anatase phase, as supported by the characteristic diffraction peaks shown in the XRD pattern in **Fig. 5A**. The samples HCS MED CO_2, and HCS HIGH CO_2 consist of a mixture of anatase and rutile phases, as evaluated by Rietveld analysis. The formation of either anatase or rutile is influenced by the size-dependency of the thermodynamic phase stability.[35, 36] For crystallites smaller than 13 nm, anatase becomes the thermodynamically stable phase, while with larger crystallite sizes, the rutile phase starts forming. Detailed values, including the crystallite sizes, are given in **Table 1**.

Thermal annealing in carbon dioxide at 800 °C tailors the carbon shell as well.[33] Carbon etching, thus partial carbon removal, with the result of additional micropore generation in the shells, increases the relative percentage of titania in the samples in the range of 47-77 mass% (determined by thermogravimetric analysis in synthetic air, **Fig. 5B**).

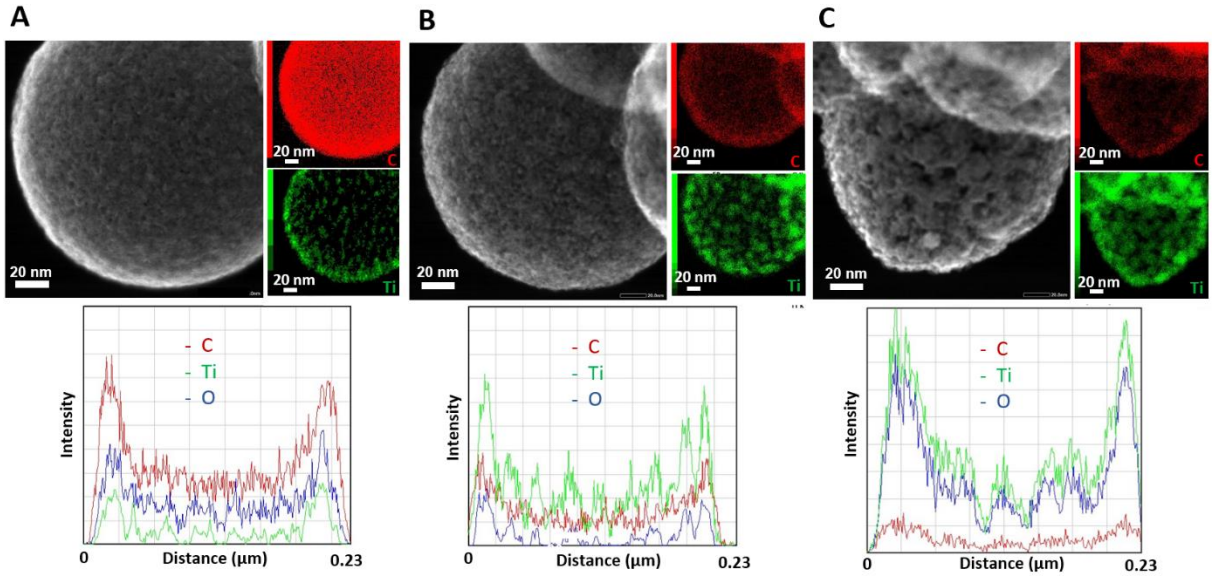

Fig. 4: Scanning transmission electron micrographs, elemental mappings, and cross-sectional elemental profiles of low (A), medium (B), and high titania loaded (C) spherogels after activation with carbon dioxide at 800 °C for 30 min.

Nitrogen gas adsorption isotherms were recorded at -196 °C to evaluate the porosity characteristics of the samples. For all samples, typical type II isotherms, according to the IUPAC classification,[37] representing a micro/macroporous morphology are obtained (**Fig. 5C**). The aforementioned titania/carbon content in the samples is directly reflected in the micropore content, dominantly present in the carbon:

Table 1: Summary of the textural properties of titania-loaded carbon spherogels after carbon dioxide activation obtained from TGA measurements, transmission electron micrographs, and nitrogen gas sorption.

Sample	**Titania content (mass%)**	**SSA (DFT) (m^2 g^{-1})**	**Titania phase and content (%) Anatase Rutile**	**Crystallite size (nm) (XRD)**	**Titania particle size (nm) (TEM)**
HCS LOW CO_2	47	1149	100 0	8 (anatase)	8
HCS MED CO_2	64	691	92 8	11 (anatase) 7 (rutile)	18
HCS HIGH CO_2	77	271	82 18	20 (anatase) 24 (rutile)	27

The highest nitrogen uptake (~ 200 cm^3 g^{-1} N_2 at STP) in micropores at relatively low pressures is observed for the low-titania-loaded sample due to the highest carbon content. A pronounced decrease is observed for the medium and high-titania-loaded samples, which contain 36 mass% and 23 mass% carbon, respectively. The corresponding specific surface areas, calculated by applying the 2D-NLDFT method for heterogeneous surfaces, are as high as 1149 m^2 g^{-1} for the low-titania loaded sample and decrease to 271 m^2 g^{-1} (**Table 1**) according

to the decrease of the carbon content. Typically, large macropores (e.g., sphere interiors of 230 nm diameter), encapsulated by a microporous carbon shell with pore diameters < 6 nm, show a pronounced hysteresis effect due to cavitation.[38] We interpret the absence of this effect as the presence of a high amount of titania (> 47 mass%), which is blocking the pathway for nitrogen desorption. Corresponding pore size distributions are shown in **Fig. S6**. While the micropore size is similar for all samples, the cumulative depiction reveals the increase in carbon content from "High" to "Low".

In addition to the increased surface area, another important feature of the CO_2 activation is the possibility of avoiding the TiO_2-to-TiC transition, thus stabilizing the TiO_2 phase either as anatase and/or rutile polymorph. The Raman spectra (**Fig. 5D**) confirmed for all HCS CO_2 samples that the nature of the carbon shell is undisturbed by the CO_2 processing as well as the TiO_2 content as displayed by the typical coeval appearance of D-mode (~1345 cm^{-1}) and G-mode (~1597 cm^{-1}) signals, which are distinctive bands of disordered, sp^2-hybridized carbon materials (*Supporting Information,* **Table S1**).[39] All HCS CO_2 samples feature a peak area ratio (A_D/A_G) of approximately 2.5 and thus reveal an incomplete crystalline characteristic with a large contribution of amorphous carbon, similar to other resol-based carbon aerogels.[39] Additionally, the disordered carbon structure is also marked by a broadening of the D-band and G-band, which were evaluated by cumulative fitting after deconvolution into five bands, namely D, D*, D**, G, and D' (*Supporting Information*, **Fig. S9**).[40, 41] The overlapping of the D' peak with the G peak, and associated also with the presence of the D peak as a typical signature of disorder and defects in graphitic materials. The four Raman modes in the range of 150-650 cm^{-1} verify the presence of titania (predominantly anatase; *Supporting Information,* **Table S2**) in all samples.[30, 42]

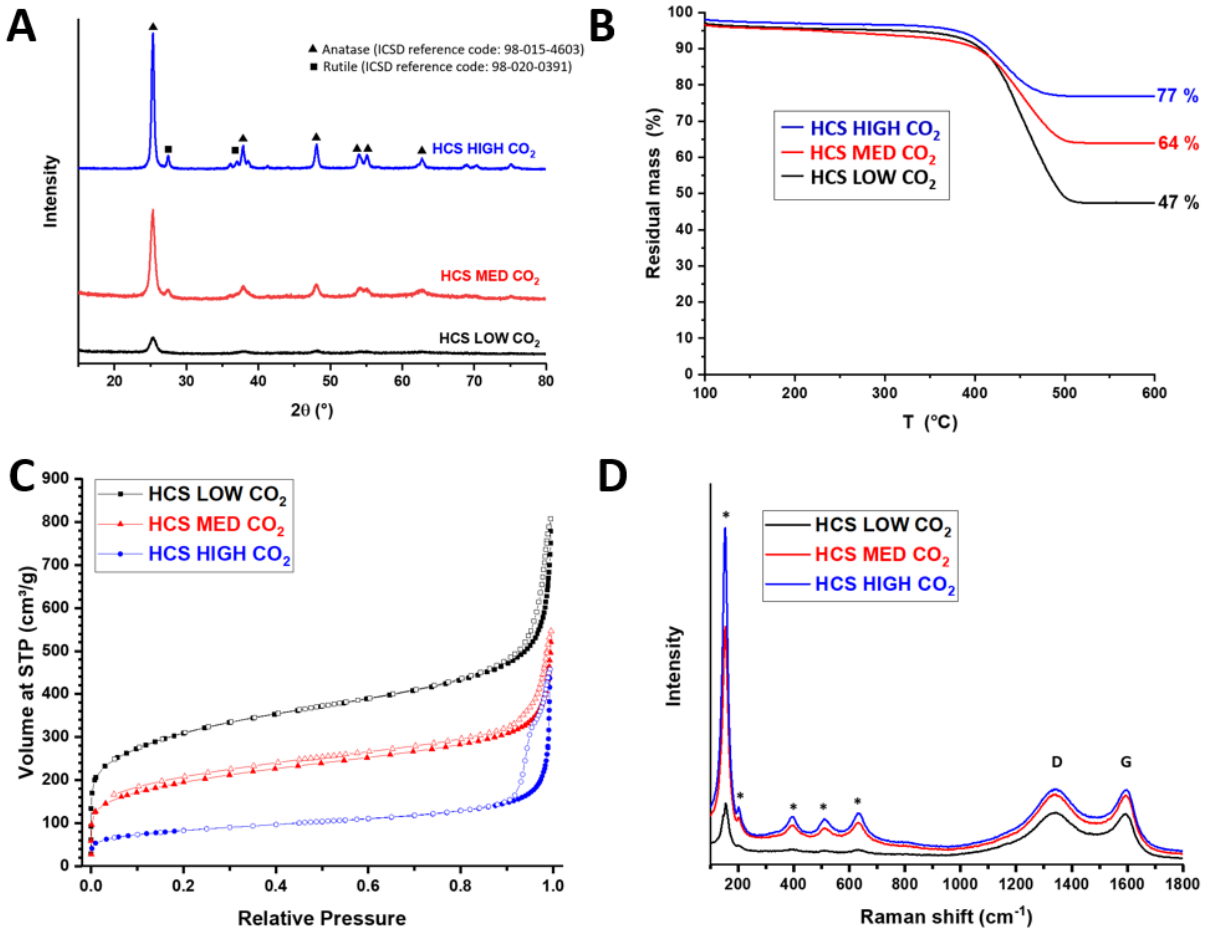

Fig. 5: Chemical and physical analysis of three different titania-loaded carbon spherogels (LOW, MED, and HIGH) after activation with carbon dioxide at 800 °C (A) X-ray diffraction patterns; (B) thermogravimetric analysis under synthetic air; (C) nitrogen sorption analysis; (D) Raman spectra (titania modes marked by asterisks[30, 42]).

Photocatalytic hydrogen evolution

The photocatalytic performance of the CO_2-activated, TiO_2-loaded carbon spherogel samples was evaluated towards light-driven H_2 generation from water splitting (i.e., hydrogen evolution reaction, HER) and compared to that of the as-prepared spherogels as well as the reference 1100 °C/Ar sample series. To minimize the effect of parasitic carbon absorption (*Sup-*

porting Information, **Fig. S7**), we employed a narrow-band UV illumination source with emission centered at 365 nm aiming to trigger band-to-band excitation in TiO_2 as the main source for photogenerated electrons.

Fig. 6A summarizes the photocatalytic H_2 generation rates measured using a batch reactor for the series of as-prepared and Ar- and CO_2-treated HCS samples with different TiO_2 contents. The as-prepared C/TiO_2 samples show only marginal H_2-evolution rates (0.0038-0.0048 µmol h^{-1}), which we relate to the encapsulation of the TiO_2 surface (required to release the photogenerated charges at the solid/liquid interface) by a dense carbon layer. The annealing of the samples at 1100 °C in Ar results in an even poorer HER performance between 0.0012 µmol h^{-1} and 0.0021 µmol h^{-1}. Based on transmission electron micrographs and X-ray diffraction data (*Supporting Information*, **Fig. S5**), the high-temperature treatment leads to the growth of TiO_2 crystallites accompanied by their conversion to HER-inactive TiC. In strong contrast to the as-prepared and Ar annealed samples, CO_2 activation of HCS composites results in encouraging H_2 generation rates that are 2-3 orders of magnitude higher (**Fig. 6A**). The level of activity of the HCS CO_2 samples is further validated using a flow-type HER reactor, as demonstrated by the as-obtained on-steam H_2 evolution profiles shown in **Fig. 6B**. Based on the insights of our comprehensive morphological and structural investigations (**Fig. 5**), these HER rates can be assigned to the partial etching of the carbonaceous shells during the CO_2 activation: it renders the TiO_2 surface accessible to the reactants in the liquid phase allowing for efficient utilization of photoexcited charge carriers.

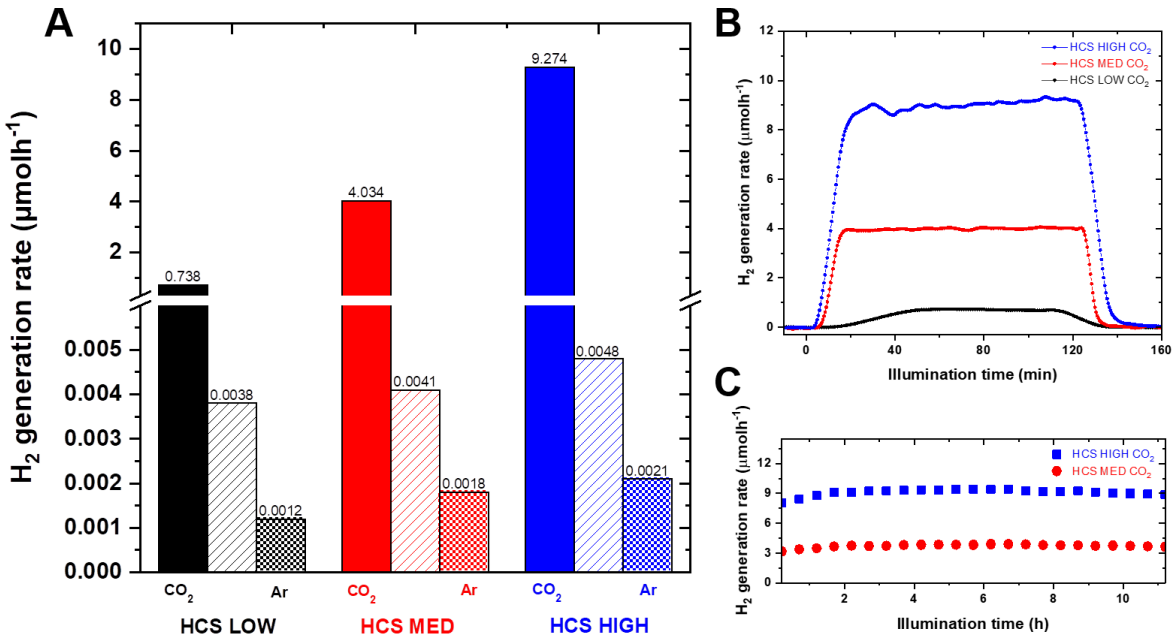

Fig. 6: Rates of H_2 evolution obtained for the as-prepared (hatched bars), 1100 °C annealed (half-tone bars), and CO_2-activated (full bars) C/TiO_2 spherogel composites (A), H_2 evolution profiles measured for the CO_2 activated composites with low, medium and high TiO_2 contents, (B) and H_2 generation rates plotted as a function of illumination time measured in long-term HER experiments exemplifying the most active spherogel photocatalysts with medium (64 mass%) and high (77 mass%) TiO_2 contents (C).

Fig. 6A provides further details on the TiO_2-content-depending performance (dashed lines). There is a noticeable increase in H_2-generation rates for samples with higher TiO_2 contents independent of the treatment applied (for as-prepared, 1100 °C, and CO_2-treated samples. The trend is highly non-linear as a function of TiO_2 amount (exemplified in *Supporting Information*, **Fig. S8**), suggesting that not only the increasing amount of absorption and catalytic centers (i.e., TiO_2 content) but also the accessibility of the carbon shell as well as the presence of anatase/rutile mixed-phase (82-92 mass% anatase and 8-18 mass% rutile; **Table 1**) contribute to the overall performance. Such intrinsic anatase/rutile junctions were shown to be beneficial for the performance of composites as they facilitate spatial charge separation.[43] We

have explored higher TiO_2 loadings as well (up to 95%). However, we have observed that the as-prepared materials became unstable and did not maintain the desired morphology. Apparently, there is an upper limit for addition of organometallic precursor amounts in the RF sol-gel process with the result of inhomogeneous samples. It turns out that a certain amount (at least 10-20%) of carbon (acting as a binder) is necessary to allow for the formation of our hybrid spherogels. The highest activity value of around 9 μmol h^{-1} is achieved for the HCS HIGH CO_2 sample despite its lowest surface area (271 m^2 g^{-1}, **Table 1**). This value can be translated to HER activity of more than 9 mmol h^{-1} g^{-1} and constitutes one of the highest mass-normalized rates compared to other C/TiO_2 based nanostructures reported elsewhere.[9]

Given the simplicity of the HCS composite fabrication and the ease of C-to-TiO_2 content control, we were next interested in the long-term HER performance and stability of the prepared photocatalysts under turnover conditions. Following the short-term flow-type H_2 evolution experiments discussed above, **Fig. 6C** shows overnight HER runs featuring the most active HCS MID CO_2 and HCS HIGH CO_2 composites. Both materials demonstrate stable performance (i.e., constant rates of H_2 evolution) without any apparent deactivation for at least 10 h of uninterrupted illumination, which commends these composites as robust and efficient photocatalysts for H_2 production.

The best-performing HCS HIGH CO_2 was investigated after the photocatalytic HER run to elaborate on its integrity. **Fig. 7A-B** shows a collection of micrographs obtained for the samples recovered from the reaction solution. Several main observations can be highlighted. First, compared to neat HCS HIGH CO_2 (**Fig. 4**), the sample HCS HIGH CO_2 shows no severe changes in its morphology: both the size of TiO_2 crystallites and the structure of the carbon layer seem intact. Second, transmission electron microscopy reveals that the preferred location of Pt na-

noparticles (used here to provide HER sites) is on the outer shell of titania-encapsulating carbon (**Fig. 7B**). This observation suggests that the carbonaceous shell is sufficiently conductive and allows effective extraction of the electrons from TiO_2 to the active H_2 generation centers on Pt. Based on this, we can conclude that the main factor allowing for the high HER performance of the CO_2-activated HCSs is likely related to the effective consumption of photogenerated holes (scavenging by MeOH) at the TiO_2/solution interface, which is made available during the CO_2-etching process. Finally, based on the post-mortem analysis, we can also confirm the stability of the spherogel-like meta-structures that we believe govern the properties of these versatile nanomaterials.[18, 31] Neither the UV illumination nor the ultrasound treatment or long-term stirring resulted in any significant structural collapse of the C/TiO_2 spheres, which one more time emphasizes their excellent stability.

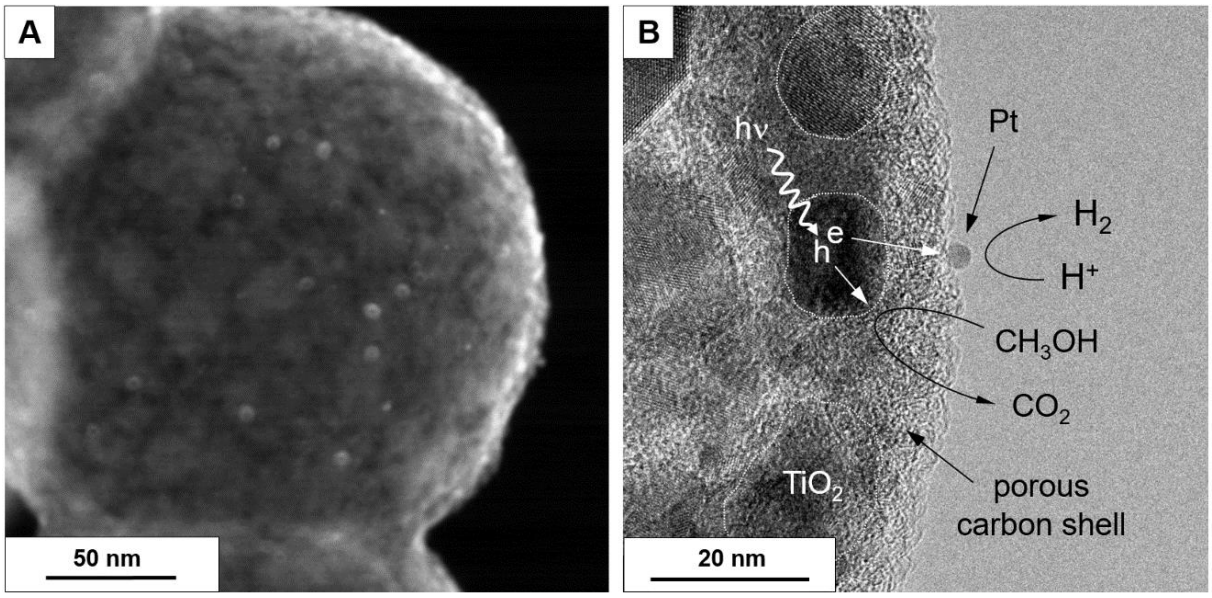

Fig. 7: Post mortem TEM analysis of Pt-loaded hybrid spherogel samples demonstrates the intact morphology of the spherogels after the catalytic run (A): Pt can be seen as bright nanoparticles decorating the C/TiO_2 spheres. Magnified view of a single sphere's edge showing a collection of TiO_2 nanocrystals (highlighted with dashed white lines) embedded into a carbon

shell which is rendered porous during the CO_2-activation (B): photodeposition of Pt nanoparticles on the outer part of the shell suggests that the electrons excited in TiO_2 are released at the C/solution interface; the superior photocatalytic performance of the samples after CO_2-activation thus suggests the release of photoexcited holes at the TiO_2/solution interface to be the major factor limiting the performance of the as-prepared HCSs.

Conclusions

We introduce a versatile synthesis method to obtain hollow-core carbon spheres with high mass loading of titania. Our aqueous route to generate titania hybrid carbon spherogels allows for high morphology control via PS sphere templating. Therefore, it is essential to use a suitable water-soluble Ti-precursor and carefully adjust reaction parameters such as templating amount, pH value, and RF dilution ratio. Titanium(IV) bis(ammonium lactate) is an ideal candidate, allowing titania loadings, solely arranged in the hollow carbon spheres, in the range of 30-60 mass%. Compared to silica-templating approaches, which commonly need hydrofluoric acid to generate hollow carbon sphere materials, we benefit from an easy, thermally triggered template removal during carbonization. The existence of a wide variety of transition metal lactates evokes great promise to enlarge our strategy for encapsulating many other metal oxides into carbon.

Physical activation with carbon dioxide, typically a powerful tool to tailor the micropore nature of carbons, allows for the present materials and adjustment of the titania content and its particle growth. This post-synthesis treatment is further shown to be essential to render the spherogels highly active photocatalysts for hydrogen evolution reaction. Our experiments show that the thickness of the carbon layer and its partial etching via CO_2-activation control the performance, which we associate with the degree of TiO_2 surface accessibility. This activation turns our hybrid spherogels into promising future photocatalysts comparable to other graphene/carbon nanotube-TiO_2 materials.

Declaration of competing interest

The authors declare that there are no conflicts of interest.

Acknowledgments

This research was financially supported by the Salzburg Center for Smart Materials (P1727558-IWB01), which is funded by the European Funds for Regional Development (EFRE) and the Austrian Wirtschaftsservice (AWS). M.S. is grateful for receiving the DOC Fellowship of the Austrian Academy of Sciences (ÖAW). Moreover, the authors acknowledge that the JEOL JEM F200 TEM instrument was funded by Interreg Österreich-Bayern 2014−2020 Programm- AB29 "Synthese, Charakterisierung und technologische Fertigungssätze für den Leichtbau" n2m "(nano-to-macro)". The INM authors thank Eduard Arzt for his continuing support. AC and SM acknowledge research funding by the Austrian Science Fund (FWF) P32801-N. Furthermore, the authors acknowledge the financial support for the DXR2 Raman microscope provided by the European Regional Development Fund and Interreg V-A Italy Austria 2014–2020 through the Interreg Italy-Austria project ITAT 1023 InCIMa "Smart Characterization of Intelligent Materials" and the Interreg Italy-Austria project ITAT1059 InCIMa4 for Science and SMEs project.

Associated content

Supporting Information

Figure S1: SEM and DLS analysis of polystyrene templates; Figure S2: TEM images of various pH values and PS concentrations; Figure S3: Thermogravimetric analysis of low, medium, and high-titania-loaded carbon spherogels; Figure S4: STEM EDX of low, medium, and high-titania-loaded carbon spherogels; Figure S5: TEM image and X-ray diffraction of a titanium carbide loaded carbon spherogel sample (thermally treated up to 1100 °C under Ar); Figure S6: Pore size distributions for three different titania-loaded carbon spherogels (LOW, MED, and HIGH) after activation with carbon dioxide at 800°C; Figure S7: DRS data of HCS HIGH CO_2 sample; Figure S8: H_2 evolution rates depending on the titania loading; Figure S9: Deconvolution and cumulative Raman fit of D- and G-bands; Table S1 and S2: Raman peak analysis

TOC (For Table of Contents Use Only)

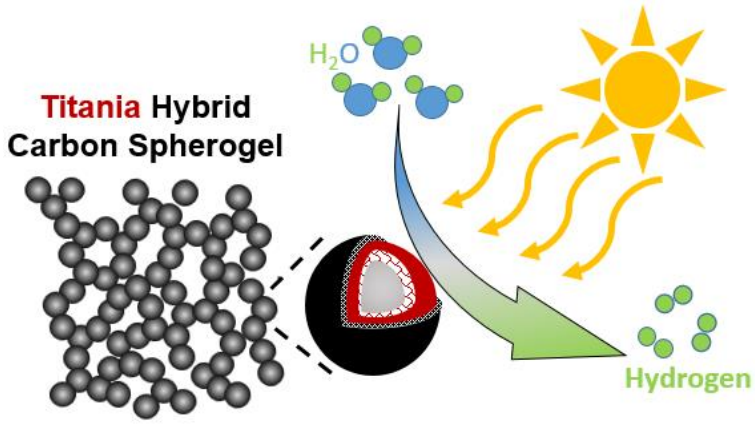

References

1. S. Chu and A. Majumdar, *Nature*, 2012, **488**, 294-303.
2. J. Rockström, O. Gaffney, J. Rogelj, M. Meinshausen, N. Nakicenovic and H. J. Schellnhuber, *Science*, 2017, **355**, 1269-1271.
3. M. Momirlan and T. N. Veziroglu, *International Journal of Hydrogen Energy*, 2005, **30**, 795-802.
4. S. Hui, L. Shunqin, H. Hengming, D. Bowen and YeJinhua, *ACS Energy Letters*, 2022, **7**, 1043.
5. M. Suss, Y. Zhang, I. Atlas, Y. Gendel, E. Ruck and V. Presser, *Electrochemistry Communications*, 2022, **136**, 107211.
6. H. Song, S. Luo, H. Huang, B. Deng and J. Ye, *ACS Energy Letters*, 2022, **7**, 1043-1065.
7. M.-M. Titirici, R. J. White, N. Brun, V. L. Budarin, D. S. Su, F. del Monte, J. H. Clark and M. J. MacLachlan, *Chemical Society Reviews*, 2015, **44**, 250-290.
8. P. Lanzafame, G. Centi and S. Perathoner, *Chemical Society Reviews*, 2014, **43**, 7562-7580.
9. N. R. Reddy, U. Bhargav, M. M. Kumari, K. Cheralathan and M. Sakar, *International Journal of Hydrogen Energy*, 2020, **45**, 7584-7615.
10. K. Gregorczyk and M. Knez, *Progress in Materials Science*, 2016, **75**, 1-37.
11. N. Kemnade, P. Gebhardt, G. M. Haselmann, A. Cherevan, G. Wilde and D. Eder, *Advanced Functional Materials*, 2018, **28**, 1704730.
12. S. Fleischmann, A. Tolosa and V. Presser, *Chemistry–A European Journal*, 2018, **24**, 12143-12153.
13. M. Naguib, O. Mashtalir, M. R. Lukatskaya, B. Dyatkin, C. Zhang, V. Presser, Y. Gogotsi and M. W. Barsoum, *Chemical Communications*, 2014, **50**, 7420-7423.
14. O. Budak, M. Geißler, D. Becker, A. Kruth, A. Quade, R. Haberkorn, G. Kickelbick, B. Etzold and V. Presser, *ACS Applied Energy Materials*, 2020, **3**, 4275-4285.
15. H. Liu, W. Li, D. Shen, D. Zhao and G. Wang, *Journal of the American Chemical Society*, 2015, **137**, 13161-13166.
16. R. J. White, K. Tauer, M. Antonietti and M.-M. Titirici, *Journal of the American Chemical Society*, 2010, **132**, 17360-17363.
17. J. Liu, N. P. Wickramaratne, S. Z. Qiao and M. Jaroniec, *Nature materials*, 2015, **14**, 763-774.
18. M. Salihovic, G. A. Zickler, G. Fritz-Popovski, M. Ulbricht, O. Paris, N. Hüsing, V. Presser and M. S. Elsaesser, *Carbon*, 2019, **153**, 189-195.
19. T. Yang, Y. Zhong, J. Liang, M. M. Rahman, W. Lei, Y. Chen, M. J. Monteiro, Z. Shao and J. Liu, *Particle & Particle Systems Characterization*, 2017, **34**, 1600281.
20. D. Li, C. Feng, H. kun Liu and Z. Guo, *Journal of Materials Chemistry A*, 2015, **3**, 978-981.
21. T. Fu, X. Wang, H. Zheng and Z. Li, *Carbon*, 2017, **115**, 363-374.
22. F. Xu, Y. Lu, J. Ma, Z. Huang, Q. Su, R. Fu and D. Wu, *Chemical Communications*, 2017, **53**, 12136-12139.
23. Z. Li, J. Zhang, B. Guan, D. Wang, L.-M. Liu and X. W. D. Lou, *Nature Communications*, 2016, **7**, 1-11.
24. M. Fang, Z. Chen, Y. Liu, J. Quan, C. Yang, L. Zhu, Q. Xu and Q. Xu, *Journal of Materials Chemistry A*, 2018, **6**, 1630-1638.
25. M. Salihovic, J. Schoiber, A. Cherevan, C. Rameshan, G. Fritz-Popovski, M. Ulbricht, S. Arnold, V. Presser, O. Paris, M. Musso, N. Hüsing and M. S. Elsaesser, *Chemical Communications*, 2021, **57**, 3905-3908.
26. X. Du and J. He, *Journal of Applied Polymer Science*, 2008, **108**, 1755-1760.
27. A. Puziy, O. Poddubnaya, B. Gawdzik and M. Sobiesiak, *Adsorption*, 2016, **22**, 459-464.
28. J. Jagiello and J. P. Olivier, *The Journal of Physical Chemistry C*, 2009, **113**, 19382-19385.
29. G. M. Haselmann and D. Eder, *ACS Catalysis*, 2017, **7**, 4668-4675.
30. J. S. Schubert, J. Popovic, G. M. Haselmann, S. P. Nandan, J. Wang, A. Giesriegl, A. S. Cherevan and D. Eder, *Journal of Materials Chemistry A*, 2019, **7**, 18568-18579.
31. M. Salihovic, P. Schlee, S. Herou, M.-M. Titirici, N. Hüsing and M. S. Elsaesser, *ACS Applied Energy Materials*, 2021, **4**, 11183-11193.

32. F. Xu, Z. Tang, S. Huang, L. Chen, Y. Liang, W. Mai, H. Zhong, R. Fu and D. Wu, *Nature Communications*, 2015, **6**, 1-12.
33. M. S. Contreras, C. A. Páez, L. Zubizarreta, A. Léonard, S. Blacher, C. G. Olivera-Fuentes, A. Arenillas, J.-P. Pirard and N. Job, *Carbon*, 2010, **48**, 3157-3168.
34. B. Krüner, J. Lee, N. Jäckel, A. Tolosa and V. Presser, *ACS Applied Materials & Interfaces*, 2016, **8**, 9104-9115.
35. A. S. Barnard and P. Zapol, *The Journal of Physical Chemistry B*, 2004, **108**, 18435-18440.
36. J. Banfield, *Journal of Materials Chemistry*, 1998, **8**, 2073-2076.
37. M. Thommes, K. Kaneko, A. V. Neimark, J. P. Olivier, F. Rodriguez-Reinoso, J. Rouquerol and K. S. Sing, *Pure and Applied Chemistry*, 2015, **87**, 1051-1069.
38. M. Thommes, *Chemie Ingenieur Technik*, 2010, **82**, 1059-1073.
39. Z. Zhai, S. Wang, Y. Xu, L. Zhang, M. Yan and Z. Liu, *Journal of Solid State Electrochemistry*, 2017, **21**, 3545-3555.
40. A. Coccato, J. Jehlicka, L. Moens and P. Vandenabeele, *Journal of Raman Spectroscopy*, 2015, **46**, 1003-1015.
41. L. Bokobza, J.-L. Bruneel and M. Couzi, *C*, 2015, **1**, 77-94.
42. O. Frank, M. Zukalova, B. Laskova, J. Kürti, J. Koltai and L. Kavan, *Physical Chemistry Chemical Physics*, 2012, **14**, 14567-14572.
43. D. O. Scanlon, C. W. Dunnill, J. Buckeridge, S. A. Shevlin, A. J. Logsdail, S. M. Woodley, C. R. A. Catlow, M. Powell, R. G. Palgrave and I. P. Parkin, *Nature materials*, 2013, **12**, 798-801.